Mechanisms of non-modal energy amplification in channel flow between compliant walls

Journal:	*Journal of Fluid Mechanics*
Manuscript ID:	draft
mss type:	Standard
Date Submitted by the Author:	n/a
Complete List of Authors:	Hoepffner, Jerome; keio, mech. Eng. Bottaro, Alessandro Favier, Julien
Keyword:	Flow structure interactions < Aerodynamics

Under consideration for publication in J. Fluid Mech.

Mechanisms of non-modal energy amplification in channel flow between compliant walls

JÉRÔME HŒPFFNER[1], ALESSANDRO BOTTARO[2] AND JULIEN FAVIER[2]

[1]Dept of Mechanical Engineering, Keio University, 3-14-1 Hiyoshi, Yokohama, 223-8522, Japan.
[2]DICAT, Università di Genova, Via Montallegro 1, 16145, Genova, Italy.

(Received May 28, 2008)

The mechanisms leading to large transient growth of disturbances for the flow in a channel with compliant walls are investigated. The walls are modeled as thin spring-backed plates, and the flow dynamics is modeled using the Navier–Stokes equations linearised about the parabolic Poiseuille profile. Analysis for streamwise-invariant perturbations show that this fluid-structure system can sustain oscillatory energy evolution of large amplitude, in the form of spanwise standing waves. Such waves are related to the travelling waves which free wall can support, modified to account for an 'added mass' effect. Simple scaling arguments are found to provide results in excellent agreement with computations of optimal disturbances, for low to moderate values of the stiffness parameter characterising the compliant surface. Movies are available with the online version of the paper.

1. Introduction

The original observations by Gray (1936) of swimming dolphins, and the inference that their high propulsive efficiency is - at least partially - due to the compliance of their skin, has attracted much attention on the effect of flexible boundaries on transitional and turbulent flows. Studies on the subject started with Kramer (1957, 1960) who conducted pioneering tests by towing a torpedo-like model, equipped with an artificial skin modeled on the structure of the dolphin's dermis and epidermis, with a motor boat in Long Beach Harbor, California. Kramer's experiments could not be successfully replicated in the years to follow (giving rise to the so-called Kramer controversy), reflecting the extreme sensitivity of the problem to the properties of the compliant wall and the environmental conditions; however, the appealing idea of tailoring wall characteristics to control the fluid flowing over it did not die out, and successive waves of funding resources in Russia, the United States, some European countries and Japan were geared towards studies of optimal compliant coatings for drag reduction over aerial and marine vehicles (cf. Chapt. 7 of Gad-el Hak (2000), for an excellent overview of the subject).

From the theoretical/computational point of view, the problem is a classical fluid-structure interaction problem, with potential difficulties related to the coupling between the solver dedicated to the solid part (where the Navier equations must be used) and that used in the fluid domain (where the Navier–Stokes equations apply). An alternative is represented by the use of thin plate/shell theory to model the behaviour of the solid. When the deformation and the displacement of the bounding plate are sufficiently small, a simple linearized problem can be derived by replacing the no-slip condition on the plate's

actual boundary with equivalent boundary conditions applied over a fictitious wall. The study of the growth/decay of small disturbances developing in the flow past compliant surfaces (modeled as thin plates) has been given a strong impulse by Carpenter & Garrad (1986) and Carpenter & Garrad (1985), after the initial theories laid out by Benjamin (1960) and Landahl (1962). Carpenter and Garrad focussed on the stability of boundary layer flows over Kramer-type compliant walls. The motivation for their work was the so-called Gray's paradox which holds that the sustained swimming speed of some species of dolphin can only be maintained by the extraordinary laminar flow properties of their skins (see e.g. Carpenter *et al.* (2000)). Results demonstrated that a suitable choice of material properties could delay transition induced by viscous instabilities, but conflicting requirements on the properties of the wall coating were needed to yield appreciable positive effects on the flow-induced surface instabilities. In practical applications, the presence of wall-based instabilities (which can take many different forms) would limit the potential for obtaining a transition delay. Today, it is believed that Gray's premises were flawed (Fish & Lauder (2006)). Drag on the dolphin is not kept low by the maintenance of a laminar boundary layer; evidence indicates that streamlining of the body causes the turbulent boundary layer over the dolphin's skin to remain fully attached (with a consequent drag benefit against the separated-flow configuration). According to Fish & Lauder (2006), drag reduction is also associated to so-called behavioural mechanisms of the dolphin, related mainly to its breathing habits.

Since in many natural and technological applications involving interactions between fluids and solids, the solid is not infinitely rigid, there is scope for investigating the stability characteristics of shear flows over compliant walls. One of the most thorough analyses was conducted by Davies & Carpenter (1997) for the case of the flow in a compliant channel with perturbations having same symmetry about the centreline as the Tollmien-Schlichting waves; analytical and numerical results are reported for all possible disturbances that can appear in the system. As far as hydrodynamic modes are concerned, the paper closes with: "... it may well be possible to suppress Tollmien-Schlichting waves completely using multiple-panel compliant walls ...". On the other hand, the different surface-based instabilities were investigated by Davies & Carpenter (1997). These wall instabilities are: traveling wave flutter (TWF, due to Kelvin-Helmholtz instability), static divergence waves, and coalescing modes. It was found that the fluid layers nearest to the walls play a crucial role in stabilising TWF, and the stabilisation effect is enhanced by wall damping, i.e. when a viscous fluid substrate or viscoelastic losses are included in the wall model. Like in previous studies, it is also reported that the onset of divergence (which physically appears as a stationary or slowly traveling surface wave) is difficult to predict; for example, the authors state that divergence is unlikely to appear when coatings efficient at stabilising Tollmien-Schlichting waves are considered. Finally, many different cases of instabilities characterised by coalescing modes are reported, with strong interactions possible between TWF modes and either divergence or Tollmien-Schlichting waves, possibly leading to absolute instabilities. If perturbations with both parities about the centreline are considered (Nagata & Cole 1999; Guaus & Bottaro 2007) it is found that the antisymmetric TWF modes always become unstable before their symmetric counterparts, at least for the range of parameters considered by Davies & Carpenter (1997). We terminate this brief introduction to the literature by noting that several other studies on the modal stability of flows interacting with elastic surfaces have been conducted; for a comprehensive review the reader is referred to the book edited by Carpenter & Pedley (2003).

We would like in this paper to examine the compliant wall flow from a new perspective. The most basic question of hydrodynamic stability analysis is: 'Are there perturbations

which can grow?' The question of stability is classically answered by invoking the flow eigenmodes: if there are eigenmodes with positive growth rate, then the flow is deemed unstable. This approach is most meaningful when the long-time behaviour is of interest. On the other hand, there can be perturbations growing for intermediate times, even when all eigenmodes are damped. In this context, the basic question 'are there perturbations which can grow' is best answered using optimisation. Indeed, if the perturbation growing the most does not grow much, the flow can be deemed *insensitive*. On the other hand, if there exist initial conditions capable to provoke large disturbance energy amplification, the flow must be catalogued as *sensitive*. Further questions which then arise concern the amount by which disturbances can grow, the mechanisms responsible for the disturbance amplification and their relation with the receptivity environment. As opposed to the classical approach, involving individual eigenmodes, the analysis which focusses on the short-time behaviour of disturbances is often referred to as *non-modal*.

Transition to turbulence in boundary layers and channels has often been linked to so-called optimal disturbances, i.e. those disturbances capable of eliciting the largest amplification over a given length/time scale. The optimal growth mechanism is most often associated to the presence of streamwise streaks and vortices: it has been shown that, in shear flows bounded by rigid walls, the amplification and the subsequent breakdown of streaks is strongly related to the transient behaviour of initial perturbations (Trefethen *et al.* 1993; Schmid & Henningson 2001).

In the present paper, we conduct a non-modal study of the stability of the compliant channel flow, to assess the effect of short time amplification mechanisms, and determine similarities and differences with the rigid-wall case. Such a study is supported by the observations of large transient temporal oscillations by Domaradzki & Metcalfe (1987) in their numerical study on the stabilisation of laminar boundary layers by compliant membranes. They report long persistence of oscillations and concluded on the 'possibility of serious difficulties in predicting the secular behaviour of fully coupled systems if care is not exercised in choosing the initial conditions'. For simplicity, we consider a plane channel, with two compliant walls characterised by identical properties, and investigate growth mechanisms for sinuous and varicose symmetries of the perturbations.

2. System description

Following Carpenter & Garrad (1986), the Kramer-type wall is modeled as a spring-backed flexible plate. Its deviation η from rest at $y = \pm 1$ obeys the equation:

$$m\eta_{tt} + \frac{d}{Re}\eta_t + \frac{B\Delta_{2\mathrm{D}}^2 + T\Delta_{2\mathrm{D}} + K}{Re^2}\eta = \pm p|_{\mathrm{wall}}, \tag{2.1}$$

where the subscript t denotes derivative with respect to time, $\Delta_{2\mathrm{D}} = \partial_{xx} + \partial_{zz}$ is the two-dimensional Laplacian, x and z are the streamwise and spanwise coordinates, and the Reynolds number is based on channel half-height, centreline velocity and dynamic viscosity. The fluid pressure p forces this equation with a positive sign at the top wall and a negative sign at the bottom wall. The other parameters are the wall density m, the wall damping coefficient d, the wall flexural rigidity B, the wall tension T and the spring stiffness K (Davies & Carpenter 1997). A similar model, with however the inclusion of the normal viscous stresses in the forcing term on the right-hand-side of (2.1), has been considered, for example, by Wiplier & Ehrenstein (2001).

For this wall model, there are five parameters in addition to the Reynolds number. Since this is a large parameter space, we fix $B = 4K$, $T = 0$ and $m = 2$, following Davies & Carpenter (1997). With this choice of m, the mass of the walls is comparable to that of

the fluid (which has unit density), so that inertia of both media play a role in the system's dynamics. When considering the evolution of wave packets, the interplay of tension, flexibility and spring stiffness, T, B and K, influences the group velocity. For the present investigation on the other hand, we consider simple harmonic waves, and thus in (2.1) it is mainly the balance between the coefficients of the acceleration term η_{tt} and position, η, that affect the behaviour of wall waves. For this reason, we change the wall properties mainly by varying the spring stiffness K. We have nonetheless performed additional computations with others parameters to assess the wider relevance of our conclusions. In (2.1), the wall equation was made dimensionless on the basis of characteristic flow quantities (which explains the presence of the factors $1/Re$ and $1/Re^2$), in order to maintain constant wall physical properties while changing the Reynolds number of the flow.

The dynamics of the flow is described by the Navier–Stokes and continuity equations, linearized about the Poiseuille profile $U = 1 - y^2$:

$$\begin{aligned} u_t + Uu_x + U_y v &= -p_x + \Delta u/Re, \\ v_t + Uv_x &= -p_y + \Delta v/Re, \\ w_t + Uw_x &= -p_z + \Delta w/Re, \\ u_x + v_y + w_z &= 0, \end{aligned} \tag{2.2}$$

where u, v, w are the deviations from the base flow profile in the streamwise, vertical and spanwise directions, subscripts x, y, z denote partial derivatives in these directions, and Δ is the 3D Laplacian operator. Assuming small wall displacement from rest, the no-slip boundary conditions on u, v, w at the displaced wall can be enforced by means of inhomogeneous boundary conditions at $y = \pm 1$ through a Taylor expansion:

$$u(\pm 1) + U_y(\pm 1)\eta = 0, \quad v(\pm 1) = \eta_t, \quad w(\pm 1) = 0. \tag{2.3}$$

We now consider the system's energy, where by system we denote the flow plus the walls. The total energy is composed of the flow kinetic energy, plus the wall kinetic and potential energies. The total perturbation energy of the flow/walls system is:

$$E \triangleq \underbrace{\frac{1}{2}\int_y \overline{u^2 + v^2 + w^2}\mathrm{d}y}_{\text{Flow}} + \underbrace{\sum_{\text{bot}}^{\text{top}} \left(\overbrace{\frac{1}{2} m \overline{\eta_t^2}}^{\text{Kinetic}} + \overbrace{\frac{B\Delta_{2D}^2 + T\Delta_{2D} + K}{2Re^2}\overline{\eta^2}}^{\text{Potential}} \right)}_{\text{Walls}},$$

where the energy of both top and bottom walls is accounted for. This expression will be used in the sequel, as the term for which optimisation is sought. For a single Fourier mode in the horizontal plane, with wavenumber (α, β), the expression of the energy becomes

$$\hat{E}_{\alpha\beta} = \frac{1}{8}\int_y (\hat{u}\hat{u}^\star + \hat{v}\hat{v}^\star + \hat{w}\hat{w}^\star)\mathrm{d}y + \sum_{\text{bot}}^{\text{top}} \frac{1}{8}\left(m\hat{\eta}_t\hat{\eta}_t^\star + \frac{Bk^4 + Tk^2 + K}{Re^2}\hat{\eta}\hat{\eta}^\star \right),$$

where $\hat{u}, \hat{v}, \hat{w}$ are the complex amplitude functions in y, $k^2 = \alpha^2 + \beta^2$, and $\star$ denotes complex conjugate.

The implication of the chosen expression of the metrics to be optimised for is as follows: if the wall contribution had not been included in the definition of the energy, an initial condition with little flow perturbation but large wall deformation might be able to induce a large growth of energy, as energy stored in the wall would be released through

the boundaries. We are not interested in this type of mechanism; it is thus meaningful to use E as functional for the optimisation. The only possible source of energy for the perturbations is then the base flow. For the perturbations, energy can be transferred during the time evolution between the flow and the flexible plates through pressure and viscous work at the walls.

3. Wall waves

The mechanisms that are discussed in the following sections are related to wall oscillations. We will discuss here the properties of wall waves. A flexible plate taken by itself can sustain oscillations in the form of traveling waves. These waves are described by a dispersion relation, derived from the plate's dynamic equation. If two such plates are now used to confine fluid in a channel, the travelling wave inherent to the plate's dynamic will persist despite presence of the fluid. An associated travelling wave will be generated in the fluid, induced by the plate's motion. We will see in the present section that this coupled motion will become an eigenmode of the fuid/walls system. Of course, the exact properties of the wave will be affected by the presence of the fluid, mainly in the form of an *added mass* effect. The flow profile being dependent on the wall wavelength, this added mass effect will vary. In addition, we will be able to distinguish two different symmetries: *sinuous*, when the walls move antisymetrically with respect to the centreline, and *varicose* when the walls motion is symmetrical.

The case of a system composed of two walls, fluid in between but no mean pressure gradient is particularly interesting. First because it allows an appreciation of the presence of a fluid on the behaviour of the walls, and it constitutes a first step in the analysis of sinuous and varicose waves. Second, this intermediate case provides preliminary information on the case of transiently growing perturbations which are infinitely elongated in x (streamwise wavenumber $\alpha = 0$). In this latter case, in fact, equation (2.2) becomes

$$\begin{aligned} v_t &= -p_y + \Delta v/Re, \\ w_t &= -p_z + \Delta w/Re, \\ v_y &+ w_z = 0, \end{aligned} \tag{3.1}$$

in the (y, z) plane, so that the cross-stream flow disturbance is decoupled from the streamwise disturbance u. The evolution of u can eventually be obtained from (2.2):

$$u_t + U_y v = \Delta u/Re;$$

u is forced by v through the base flow gradient U_y. We will analyse the implications of this fact later in the paper. For the moment, we study the behaviour of waves without base flow (3.1). The velocity in the direction of propagation of the wave ($\pm z$) will be denoted *longitudinal*, and the wavenumber along this direction will be denoted k (wavelength $2\pi/k$).

Selected eigenmodes are depicted in figure 1 for the sinuous symmetry and 2 for the varicose symmetry. These flow fields correspond to waves traveling from right to left. For a sinuous wave of long wavelength, the motion of flow particles is mainly vertical, moving as a bulk with the walls (figure 1 top left). For short sinuous waves on the other hand, the flow motion occurs mostly in thin layers along the walls. We observe in figure 1 that these layers have an exponential profile with coefficient $-k$. This exponential profile can be derived on the basis of inviscid arguments; in the absence of a base flow and viscosity, the flow streamfunction ψ satisfies the harmonic equation

$$(D^2 - k^2)\psi_t = 0;$$

for short waves, we can assume an inhomogeneous boundary condition at the wall (moving wall boundary condition) and $\psi \to 0$ away from the wall. Considering the bottom wall for instance, the solution is $\psi = \varepsilon \exp[-k(y+1)+\mathrm{i}(kz+\omega t)]$. This inviscid result accounts for the fluid displacement due to wall motion, but does not satisfy the no-slip condition for the longitudinal velocity. Viscosity results in a thin Stokes layer close to the wall. This layer can be observed in figure 1 for the longitudinal velocity component.

For the varicose mode at long wavelengths, the mechanism is different. Due to symmetry, flow particles cannot move from one wall to the other, but have to move along the channel from constricted to expanded sections. The flow motion locally tends to a parabolic profile of longitudinal velocity as the wavelength is increased, with relatively small vertical velocity. For short wavelengths, similarly to the sinuous case, a fluid layer of thickness varying with exponential rate $-k$ is observed.

From this description of the wave profiles, we can now determine the added mass effect. First, using the wall dynamical equation (2.1) without fluid (free wall), we can derive the dispersion relation, relating spatial and temporal properties of the oscillatory motion. We assume a normal mode structure for η, i.e. $\eta = \varepsilon \exp[i(kx + \omega t)]$, where ω is the angular frequency and ε is the (small) amplitude. Assuming vanishing wall damping (d=0) we find

$$m\omega^2 = \frac{Bk^4 + Tk^2 + K}{Re^2}. \tag{3.2}$$

The flexible walls in this study have density $m = 2$, and the fluid density is unity. For sinuous wave at long wavelength, fluid particle move up and down, following the wall motion. The added mass must then be unity. For short wavelengths the displaced fluid mass on each wall can be estimated from the exponential profile. Averaged over a wavelength, it should scale as:

$$\int_0^1 e^{k(y-1)} \mathrm{d}y = (1 - e^{-k})/k, \tag{3.3}$$

which indeed tends to unity as $k \to 0$. For the varicose symmetry, the dependency is the same at short wavelength, with an exponential flow profile. For long wavelength, the amplitude of the longitudinal velocity from constricted to expanded regions is empirically found to scale as $1/k^2$. Based on these considerations, we deduce the added masses applicable to sinuous and varicose modes that produce the expected effects both in the limits of small and large k, *viz.*

$$\text{Sinuous: } m_a^s = (1 - e^{-k})/k, \quad \text{Varicose: } m_a^v = (1 - e^{-k})/k + 1/k^2. \tag{3.4}$$

The frequency ω obtained from (3.2) is displayed in figure 3 (right frame) for free wall waves (no fluid); in the presence of fluid, the frequency of both sinuous and varicose modes, using the added mass model just outlined is also displayed. Finally, the results are compared to the computed eigenmodes, both in the presence and absence of viscosity, to ascertain the appropriateness of the model formulated. The quantitative agreement is satisfactory.

The system's spectrum can now be characterised. The flow eigenmodes are marginally affected when compared to the rigid channel case (cf. figure 3, left frame). In addition to these modes, there are four eigenmodes that originate from the free wall traveling waves, with the eigenfrequency reduced because of an added mass effect. These are two pairs of counter-propagating waves in the channel: one pair of sinuous modes and one pair of varicose modes. The wall deformation is associated with a velocity field localised in thin layers close to the walls for short wavelengths. When considering system eigenmodes with $\alpha \neq 0, \beta = 0$, with nonzero base flow, subtler effects of wall flexibility can be found, for

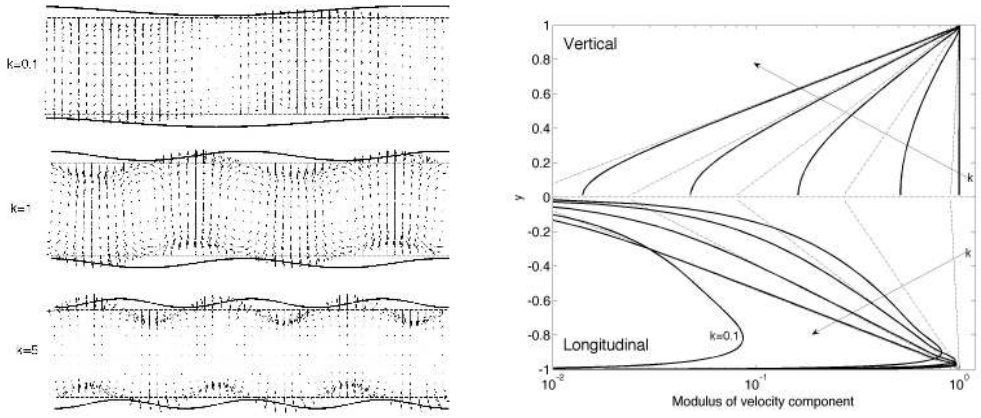

FIGURE 1. Motion of sinuous modes. Left, disturbance velocity fields for long and short wavelengths (not to scale). The waves travel from right to left. Right, vertical and longitudinal velocity components (thick solid lines), compared to exponential profiles wit exponential rate $-k$ (thin dashed lines), k varying linearly from 0.1 to 5, with $K = 10^5$, $Re = 5000$.

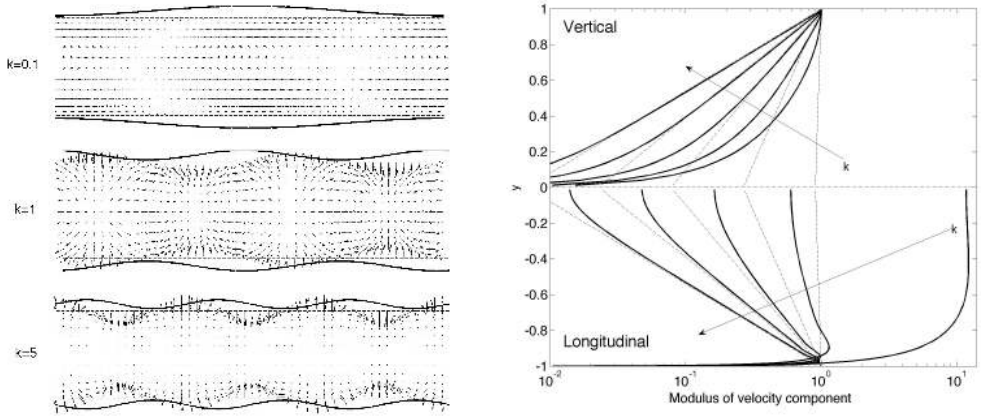

FIGURE 2. Motion of varicose modes. Left, disturbance velocity field not to scale for long and short wavelengths (not to scale). The waves travel from right to left. Right, vertical and longitudinal velocity components (thick solid lines), compared to exponential profiles with exponential rate $-k$ (thin dashed lines). The parameters are those of figure 1.

instance in the stabilisation of Tollmien-Schlichting waves (Davies & Carpenter, 1997), but for the purpose of describing the energy growth mechanism in the present paper, the understanding just provided is sufficient.

4. Optimisation results

To investigate the sensitivity of the system to external perturbations, we proceed to compute initial conditions leading to large energy growth. We will see in the next sections that the mechanism of energy growth is related to the wall traveling waves. We can thus project the system onto its least stable eigenmodes. In the following we use 30 of these eigenmodes. The projected system is then described by

$$\dot{\kappa} = \Lambda\kappa, \quad \mathcal{Q} = U^H Q U = F^H F, \tag{4.1}$$

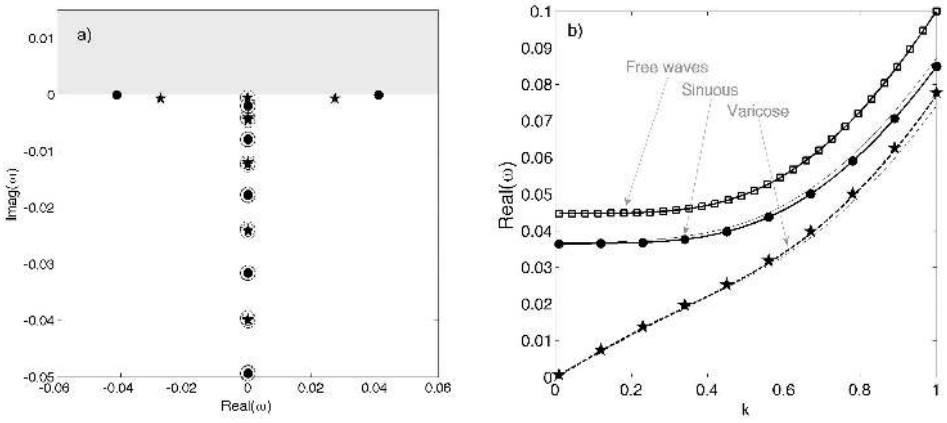

FIGURE 3. *a)* Spectrum at $k = 0.5$, for the sinuous (dots) and varicose (stars) symmetries, compared to the spectrum of the rigid system (open circles). The unstable half-plane ($\mathrm{Imag}(\omega) > 0$) is shaded. *b)*, the circular frequency ω for the free wall waves (squares), the computed eigenmodes for the sinuous wave (thick solid) and the varicose wave (thick dashed), compared to the results obtained using the added mass model (thin lines). The computed eigenmodes for the inviscid model are drawn with circles for the sinuous and with stars for the varicose symmetry (same parameters as in figure 1).

where κ is the vector of expansion coefficients of the system's state on the retained eigenfunctions (flow velocity, pressure and wall displacement), Λ is the diagonal matrix of the eigenvalues, Q is the matrix of energy weights in physical space, U the matrix whose columns are the retained eigenfunctions, $\mathcal{Q}$ is the energy weight matrix in eigenmode space (matrix of angles), and upperscript H denotes the conjugate-transpose operation. We have further factored $\mathcal{Q}$ in square root factor F. Using this formulation, we can compute for all times the maximum energy growth from an arbitrary initial condition κ_0 as

$$G(t) = \max_{\kappa_0} \frac{\|\kappa(t)\|_{\mathcal{Q}}}{\|\kappa_0\|_{\mathcal{Q}}} = \max_{\kappa_0} \frac{\|e^{\Lambda t}\kappa_0\|_{\mathcal{Q}}}{\|\kappa_0\|_{\mathcal{Q}}} \triangleq \|e^{\Lambda t}\|_{\mathcal{Q}} = \| \underbrace{F^{-1}e^{\Lambda t}F}_{\mathcal{H}} \|_2, \tag{4.2}$$

where we have used the definition of the operator norm $\|\cdot\|_{\mathcal{Q}}$, and we have expressed the $\mathcal{Q}$-norm in terms of the 2-norm using F. In this expression, the operator 2-norm can be computed as the largest singular value of $\mathcal{H}$. The worst case initial condition, that is the initial condition that maximises this growth, is associated to the first right singular vector of $\mathcal{H}$, and the response is associated to its first left singular vector; see Schmid & Henningson (2001) for further details.

A representative example of the growth envelope is shown in figure 4. We distinguish from the energy growth envelope the signature of two oscillatory mechanisms with different periods in time. The mechanism leading to the first peak arising after $t = 0$ has sinuous symmetry, with an apparent period of about 270 time units. The second mechanism has varicose symmetry, with apparent period of about 950 time units. The energy evolution of initial conditions which are optimal for target times equal to 400 and 500 are shown as dashed and dash-dotted lines. From the matching between the energy evolutions and the envelope, we can infer that the energy growth envelope is mostly due to these two particular initial conditions.

The flow fields at different times produced by these two initial conditions are displayed in figure 5. We proceed here to the qualitative description of the phenomenon; analy-

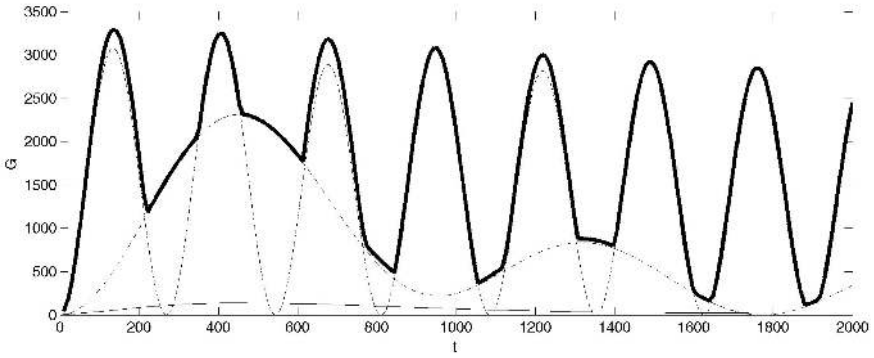

FIGURE 4. Thick line: envelope of maximum energy growth for $(\alpha, \beta) = (0, 0.2)$, $K = 10^4$, $Re = 5000$, $d = 1$. We observe two oscillatory behaviours with apparent periods $T \approx 270$ and $T \approx 950$. The energy evolution of the initial conditions optimal for $t = 400$ and $t = 500$ are represented with dashed and dot-dashed lines. The optimal growth envelope for the rigid channel at $Re = 5000$ is drawn with a thin solid line.

sis and quantification will be performed in the next section. Note that the wall motion is enforced using inhomogeneous boundary conditions at $y = \pm 1$. We have nevertheless represented the wall deformation η with thick solid lines for clarity (with arbitrary amplitude).

Initially ($t = 0$) the walls are straight and there is no streamwise velocity. The in-plane velocity profile then generates wall deformations with sinuous symmetry for the short period oscillation and with varicose symmetry for the slower process. While the walls are deformed, a streamwise disturbance velocity component is generated by vertical advection of the base flow. At peak energy time (third row of plots in the figure), the disturbance flow is mostly composed by the streamwise component of the velocity. The motion is then reversed, as an effect of the wall elasticity, until a situation close to the initial condition is reached, but with the disturbance velocity components of opposite sign. At this stage, the walls are straight again. For another apparent period of the energy curve, we observe the same process reversed (not shown). These oscillation have the structure of a *standing wave*, there is no propagation of the wall deformation in the horizontal direction ($\pm z$). When describing the energy envelopes, we referred to the *apparent* period of the oscillatory mechanisms. It is now clear that these durations were in fact half of a complete period of oscillations. Also in figure 5, only half of the oscillation is shown. We observe in figure 4 that the sinuous oscillation (of shorter period) is mildly damped, whereas the varicose oscillation is damped rapidly.

4.1. *Mechanisms for growth*

Inspection of the velocity fields of figure 5 suggests simple mechanisms for the sinuous and varicose oscillations. The discussion is now based on figure 6, where we have represented three possible oscillation scenarios: motion up and down of the entire channel and the equivalent deformations for a finite wavelength, sinuous then varicose. Considering these motions as perturbations to a static Poiseuille profile, we will quantify their energy evolution.

Let us consider first the up and down motion of the two walls (figure 6 left). A Poiseuille flow with spring-mounted walls that are slightly displaced from rest would sustain oscillations of frequency ω, with $\omega^2 = K/Re^2(m + m_a)$, due to the springs, where the mass is that of the wall plus the added mass m_a of the fluid. Denoting the wall displacement $\eta = \varepsilon \cos(\omega t)$, the parabolic velocity profile moving up and down is $u' = 1 - (y + \eta)^2$.

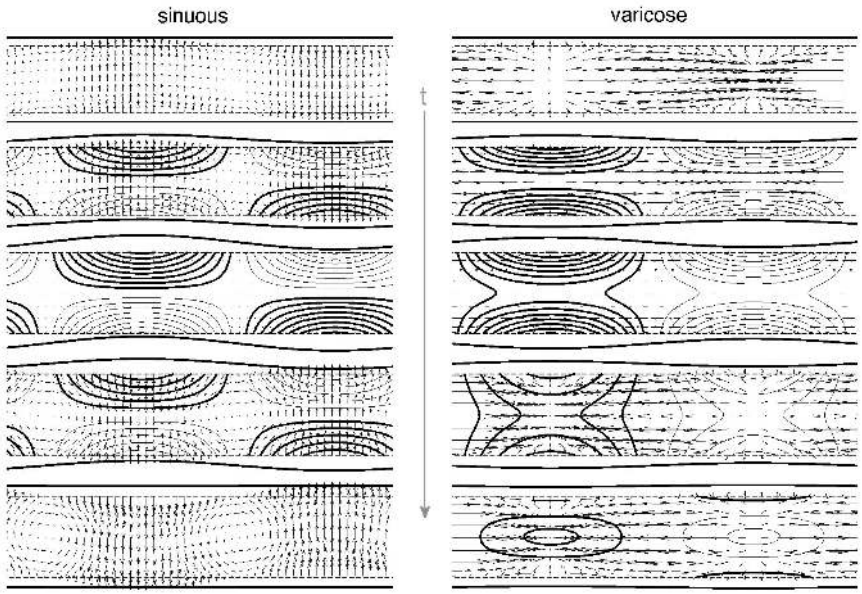

FIGURE 5. Evolution in the channel cross-section (y,z) of the sinuous (left) and varicose (right) initial conditions shown in figure 4. Snapshots at five linearly spaced instants of time (top row corresponds to $t = 0$) within the apparent oscillation period for each of these initial perturbations, v and w velocity components are represented as vector fields, and the streamwise velocity u is drawn with iso-contours: thick lines for positive velocity, and thin lines for negative (same parameters as in figure 4). Animations of the time evolution of the optimal perturbations are shown in movie 1, available with the online version of this paper.

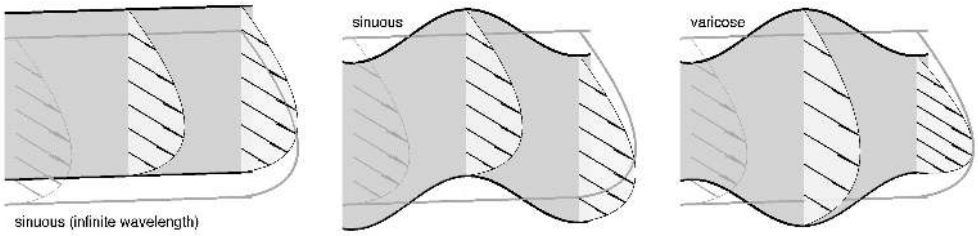

FIGURE 6. Sketch of the flow deformation induced by a spanwise standing wave. The Poiseuille base flow is displaced or stretched according to the channel deformation. Animation of these flow deformations are shown in movie 2, available with the online version of this paper.

At first order in the small displacement η the streamwise velocity is $1 - y^2 - 2\eta y$, so that the resulting time varying perturbation to the original (static) Poiseuille profile is $u(y) = -2\eta y$. The associated vertical velocity v will be constant in y at each time instant, and will be equal to the displacement velocity of the wall $v = \eta_t$ in the whole channel. In the present context, we have $w = 0$.

We can now quantify the energy evolution of this motion; the result is given below in

(4.4). The total energy is

$$E(t) = \frac{1}{2}\int_y [u'^2 + v^2]\mathrm{d}y + \left(m\eta_t^2 + K\frac{\eta^2}{Re^2}\right),$$

where we have accounted for the kinetic and potential energy of both walls. The streamwise contribution is:

$$\int_y u'^2\mathrm{d}y = \int_{-1}^{+1}\left[1-(y+\eta)^2\right]^2 dy = \frac{16}{15} + \mathcal{O}(\eta^4).$$

The 'u-portion' of the kinetic energy is thus constant in time up to order 4 in the wall displacement. Using $v = \eta_t = -\varepsilon\omega\sin(\omega t)$ we have:

$$2E(t) = \frac{16}{15} + 2\varepsilon^2\left[\omega^2(m+1)\sin^2(\omega t) + \frac{K}{Re^2}\cos^2(\omega t)\right] + \mathcal{O}(\varepsilon^4);$$

this total energy must be conserved in time, thus the coefficients of the sine and the cosine should be equal, leading to:

$$\omega^2 = \frac{K}{Re^2(m+1)}. \tag{4.3}$$

Comparing this expression with (3.2) at $k = 0$, we obtain a confirmation of the unit added mass for long-wave sinuous modes. Turning now to the perturbation energy with respect to the static Poiseuille profile, we have:

$$\int_y u^2\mathrm{d}y = \varepsilon^2\cos^2(\omega t)\int_y (2y)^2\mathrm{d}y = \frac{8}{3}\varepsilon^2\cos^2(\omega t)$$

The energy evolution of the perturbation is thus:

$$2E/\varepsilon^2 = 2\underbrace{\left(\frac{4}{3} + \frac{K}{Re^2}\right)}_{A}\cos^2(\omega t) + 2\underbrace{\left(\omega^2(m+1)\right)}_{B}\sin^2(\omega t),$$

which is the radius of an ellipse at an angle ω from its principal axis. Expressing ω as in (4.3), we obtain the energy growth along one fourth of the rotation period around the ellipse as:

$$G^s_{k=0} = \frac{A}{B} = 1 + \frac{4}{3}\frac{Re^2}{K}. \tag{4.4}$$

Despite this oscillation mechanism conserves the system's total energy, this particular perturbation to the static Poiseuille motion experiences an oscillatory energy evolution of potentially large amplitude when the walls are flexible (low K). For very large stiffness, the maximum growth tends to unity, i.e. energy conservation of the perturbation. Following the same line of thought while considering a finite wavelength, we obtain the final relation

$$G^s = 1 + \frac{4}{3}\frac{Re^2}{Bk^4 + Tk^2 + K}.$$

For the varicose case, by analogy with the sinuous case, the expression

$$G^v = 1 + \frac{14}{15}\frac{Re^2}{Bk^4 + Tk^2 + K}$$

can be selected which shows a good fit to the numerical results. The varicose case is in fact more complex, mainly due to the flow from constricted regions to expanded regions; this is discussed in more details in §5 below.

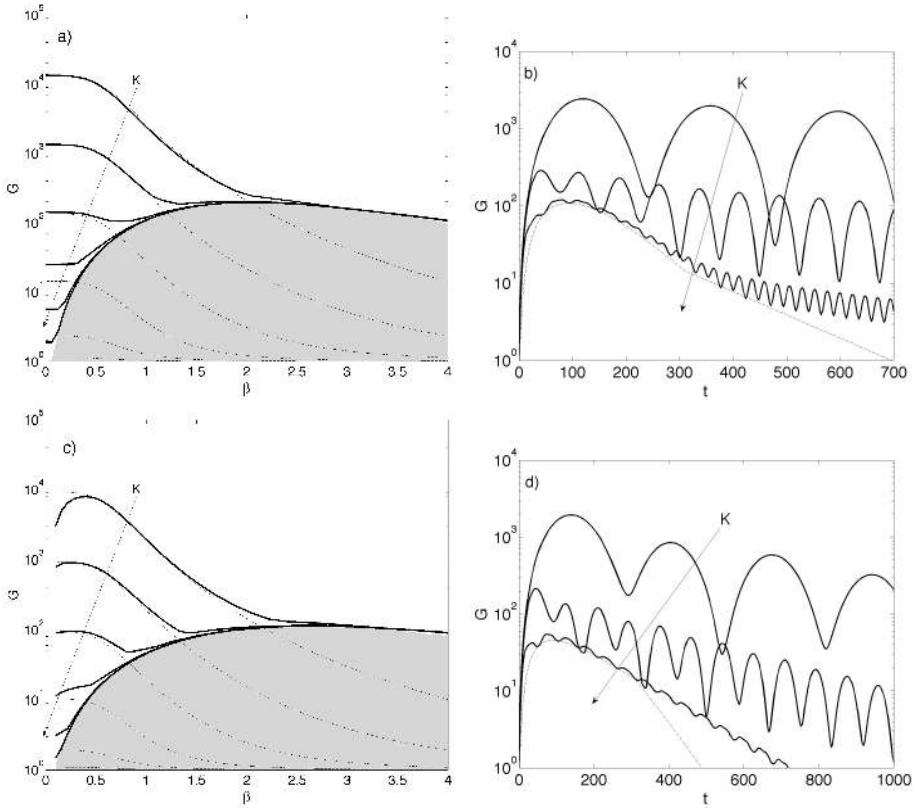

FIGURE 7. Maximum energy growth in the flexible channel for a) the sinuous and c) the varicose mechanisms while varying the spanwise wavenumber β (thick solid) and for $\alpha = 0$, $K = 10^2, 10^3, \ldots, 10^7$. The results are compared to the oscillatory model (thin dashed), and to the maximum growth of the rigid channel case (shaded area). In b) and d) the energy envelopes for sinuous and varicose modes are represented at $\beta = 1$, $d = 0$, $Re = 1000$ for $K = 10^2$, 10^3 and 10^4, and compared to the optimal envelope for the rigid channel (dashed).

In the numerical computations of the maximum transient growth we decouple the sinuous and varicose mechanisms (*cf.* Trefethen (2000) §11 for a description of how to enforce numerically this symmetry). On figure 7 the maximum growth for $\alpha = 0$ is shown for the sinuous parity. The energy growth of the rigid channel is also represented, depicted by the outer envelope of the shaded region. We can see that the model agrees well with the computed results, and that when the described mechanism leads to a lesser growth than that of the rigid system, the flexible channel gives the same result as the rigid one.

The equivalent result for the varicose symmetry is represented in figure 7c,d. For this case, the growth is compared to that of the rigid channel with imposed varicose parity (u is symmetric, v is antisymmetric about the channel centreline). Similarly to the sinuous case, we see that the oscillatory model agrees well with the computed results, and that the flexible channel tends to behave as the rigid one whenever the rigid channel allows larger growth. Note that the transient growth in the channel with varicose symmetry, corresponds to the second singular value of the propagator $\mathcal{H}$ in the case of no parity enforced a-priori.

5. The role played by wall modes in the optimal growth

We introduced this paper by justifying the need for a *non-modal* analysis. In fact we will see in this section that some eigenmodes, namely those eigenmodes which correspond to wall traveling waves, play a central role in the standing wave mechanism. Surprisingly, the role of a pairs of wall eigenmodes will be fully appreciable only when considering eigenmodes of the inviscid system.

First, we rewrite the disturbance equations in the inviscid limit:

$$\begin{aligned} u_t + U_y v &= 0, \\ v_t \qquad &= -p_y, \\ w_t \qquad &= -p_z, \\ v_y + w_z &= 0, \end{aligned} \tag{5.1}$$

with boundary conditions $v = \eta_t$ at the compliant walls; note that slip boundary conditions apply at the walls for u and w. The evolution of the v and w perturbation velocity components is that of a channel without base flow, subject to incompressibility and no-penetration at the walls. The streamwise velocity does not influence the behaviour of v and w, but since $u_t = -U_y v$, one can find the evolution of u from knowledge of v.

The flexible channel can sustain four propagative modes, arising from the free-wall case but with an added mass effect: two modes propagating in one direction, one sinuous and one varicose, and by symmetry two modes propagating in the opposite direction. We now consider two modes of one parity, propagating along $\pm z$. Owing to the symmetry ($w \to -w, z \to -z$) in (5.1), the two waves propagating in opposite directions will generate precisely the same streamwise velocity u due to the advection process discussed in the previous section. As they travel in the $\pm z$ direction, the associated u will as well propagate. Combining the two traveling waves into a standing wave, we obtain a mechanism for cancellation/superposition of the streamwise velocity: in the in-phase/out-of-phase process of the two propagating modes, the associated u will be added, then cancelled, periodically, leading to the observed oscillatory growth.

We now consider the amplitude of the u velocity generated by each traveling wave individually, basing the discussion on (5.1). For a single eigenmode of frequency ω we have:

$$i\omega\hat{u} + U_y\hat{v} = 0 \quad \Rightarrow \quad \|\hat{u}\| = \frac{T^2}{4\pi^2}\int_y |U_y\hat{v}|^2 \mathrm{d}y, \tag{5.2}$$

where $\|\hat{u}\|$ is the norm of the disturbance velocity, and $T = 2\pi/\omega$ is the period of the oscillation. In the case of cancellation/superposition effect of two counter-propagating traveling modes, the growth amplitude in $\|u\|$ will scale as T^2, that is, the slower the oscillation the larger the growth. Indeed, for an eigenmode with long time period, v will advect the base flow velocity for a long time, generating strong perturbations, before reversing its advection direction. The growth in u will depend also on the eigenmode shape $\hat{v}$, whether its support is located where large shearing $|U_y|$ is present. Note that to derive an estimate of the total energy oscillation in this standing wave process, we should as well account for the kinetic and potential energies of the wall.

To evaluate the role played by each eigenmode in the energy growth, we perform the optimisation by increasing successively the number of selected eigenmodes, from 1 to 20; starting with the least stable ones. The results are shown in figure 8. For the sinuous case at long wavelength, two modes give the full growth. The flow evolution is that of a standing wave: the two wall modes have equal amplitude. For shorter wavelength more eigenmodes must be included. For the varicose symmetry, even at long wavelength the

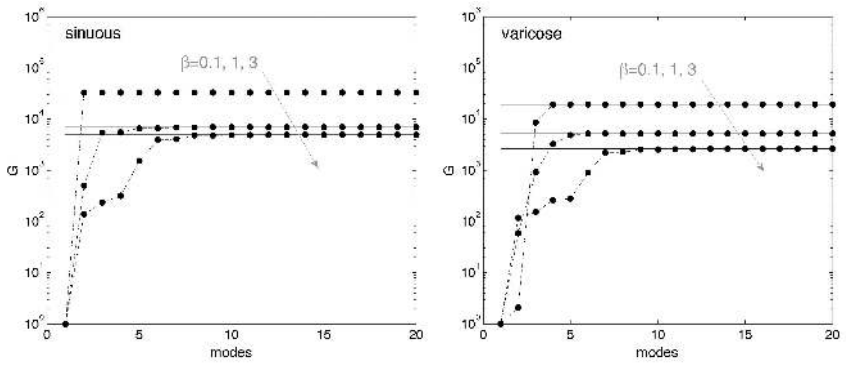

FIGURE 8. Optimal growth obtained by projection on an increasing number of eigenmodes for $K = 10^3$, $Re = 5000$.

two wall modes cannot sustain the full growth, and two additional eigenmodes must be included. It is interesting to note that one of these modes has zero wall deformation (not shown here). We can also confirm from this figure that computing the optimal growth by projecting on the 30 least stable eigenmodes is enough to obtain converged results†.

Figure 8 show that it is only for the sinuous symmetry at long wavelength, that two wall modes can form a standing wave strong enough to reproduce the optimal growth. Since the mechanisms highlighted in §4.1 are in essence inviscid, one might suspect that it is rather the eigenmodes of the inviscid system which could generate the growth when associated in a standing wave.

We compute the energy growth from a standing wave built from two oppositely propagating wall modes, based on the eigenmodes of the viscous system, and compare it with that produced by the same two eigenmodes of the inviscid system. The energy evolution is oscillatory, the maximum growth being the ratio of the maximum over the minimum energy in the course of these oscillations. The results are shown in figure 9. The energy growth curves obtained from the viscous eigenmodes (dashed curves) are consistent with results displayed in the previous figure: two modes underestimate the full growth for moderate β except for the sinuous case at low β. On the other hand, inviscid eigenmodes follow the trend of the oscillatory growth, except for the varicose case at long wavelengths. We saw that when the spanwise wavelength is long, the varicose modes generate a large flux from constricted to expanded sections, as opposed to the sinuous mode for which at long wavelength flow particles just move up and down following the wall. This effect has two consequences, the first one being a large added mass effect in the sinuous case; the oscillation/propagation is slow for the long varicose waves, and this large flux induces strong viscous losses. Based on (5.2), slow oscillations should induce large energy growth; this is observed in figure 9 when viscosity is neglected.

† Incidentally, we observe that we have been unable to obtain convergence towards the optimal solution when increasing too much the number of modes used in the projection. For example, by using the whole spectrum of eigenmodes the optimal initial condition suffers from severe dispersion errors, with numerical point-by-point oscillations. Attempts to regularise the objective function by introducing high-order derivatives of the velocity components did not yield the hoped-for smoothing of the numerical oscillations. Presumably the errors are due to the way the wall deformation is introduced in the system, by enforcing implicitly the inhomogeneous boundary conditions, but we have no definite evidence of this.

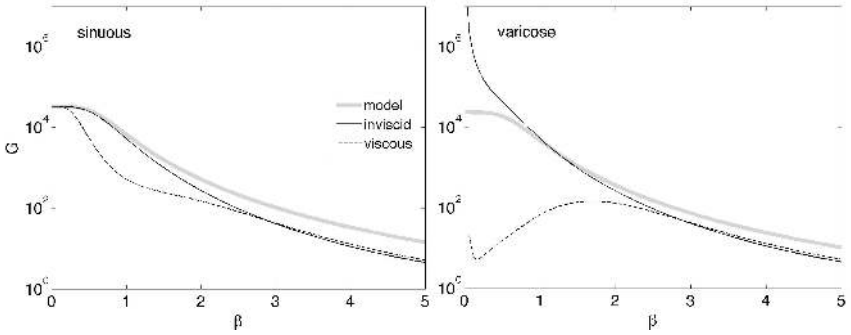

FIGURE 9. Energy growth for a standing wave composed of two oppositely propagating wall modes. Results are obtained from the eigenmodes of the inviscid case (dark solid) and viscous case (dark dashed), and are compared to the growth from the oscillatory model (light grey) already employed for the comparisons presented in figure 7. The parameters are $K = 10^3, Re = 5000$.

6. The case $\alpha \neq 0$

The case of wavenumbers with $\alpha = 0$ is favourable to energy exchange between the base flow and the perturbations, since v, w are free to evolve and u is generated by vertical advection of the base flow. When α is increased from zero in the flexible channel, relation (3.2) yields a different phase speed, affecting the interplay of the natural traveling waves and the associated pressure field near the wall. The resulting phase shift tends to attenuate the upstream propagating mode and destabilise the downstream mode, both for sinuous and varicose symmetries. This topic of flow related surface instabilities has been widely studied and we refer to Riley *et al.* (1988) for an in-depth discussion.

In this section, we compare the optimal growth to the modal instability. We will see that for long wavelengths, the mechanisms described in the previous sections dominate and that even when the modal instability is strong, transient growth plays a role of rapid amplification of the most unstable eigenmode. The neutral curves in the wavenumber plane are represented in figure 10. The unstable domain shrinks while the spring stiffness is increased, tending toward the neutral curve of the rigid channel (shaded area) for large K.

To be able to compare the optimal and modal behaviour, we consider short time optimals in figure 11*a*. Maximum growth obtained in the time interval $t \in [0, 20]$ is represented in the wavenumber plane (α, β). Despite this short time horizon, we see that at $\alpha = 0$, the oscillatory mechanism dominate. This growth is compared to that of the rigid-walls channel (thin solid). As seen in figure 7, when β increases, the flexible channel tends to behave as the rigid one. When α is not zero, the symmetry between the counter-propagating wall waves is lost, thus affecting the strength of the stationary wave mechanism. This effect can be observed for instance for $\beta = 2$ and 3.

Increasing α leads to modal instability. A large peak of exponential growth can be observed for α about one and low β. Naturally, the optimal growth is even larger. Time evolution of the growth is represented in figure 11*b* for $\beta = 0$. For long wavelengths, the start of the oscillatory growth is observed, whereas for shorter wavelengths, after an initial transient, the energy amplifies according to the least stable eigenmode. In Butler & Farrell (1992), it is shown that the initial condition which optimally transfers energy into an eigenmode is not the eigenmode itself, but its adjoint. This is what we can observe here. This initial mechanism is such that modal instability and transient growth are combined to lead to the largest possible amplification. This effects is also responsible for

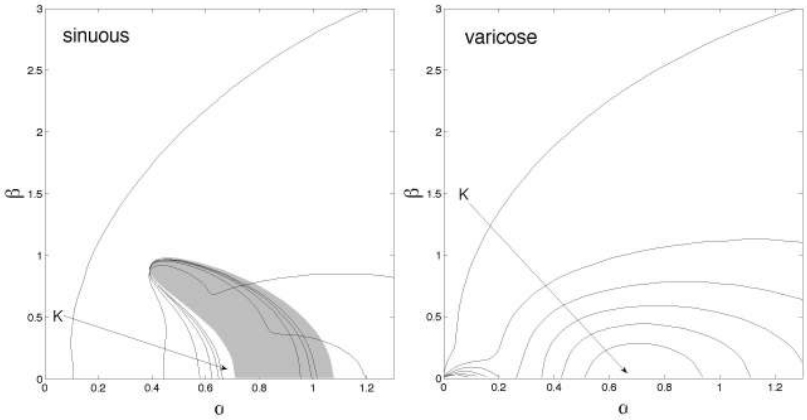

FIGURE 10. Neutral curves for spring stiffness K logarithmically spaced from 10^6 to 10^8 at $Re = 15000$. The shaded area corresponds to unstable TS waves in the rigid channel.

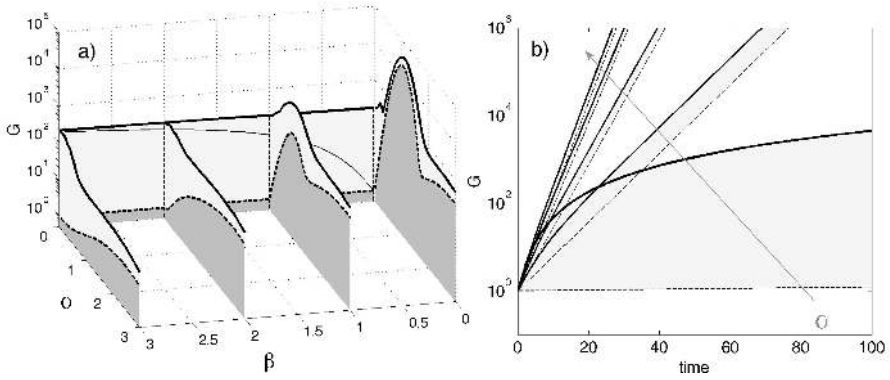

FIGURE 11. *a)* Optimal (thick solid) and exponential (dashed) growth at time 20, compared to optimal growth of the rigid-walls system at $\alpha = 0$ (thin solid) for $K = 1000, Re = 5000$. *b)* Optimal (thick solid) and exponential growth (dashed) in time for $\beta = 0$ and α equispaced from 0.01 to 1.

the peak at nonzero α of the energy growth depicted for $\beta = 1$. Inspection of the flow fields does not show standing wave oscillations. Instead upstream tilted flow structures similar to those observed by Butler & Farrell (1992) at $\beta = 0$ interact with the base flow convection with an effect of rapid transfer of energy toward the most unstable eigenmode.

7. Conclusions

We have aimed at answering the question: 'Are there perturbations that can grow in a compliant channel?' and have indeed found three mechanisms: two spanwise standing wave oscillation processes, one sinuous (wall deformed antisymmetrically with respect to the channel centreline) and one varicose (walls symmetrical), plus one mechanism similar to that of the rigid channel: generation of streamwise streaks due to streamwise elongated vortices (also known as lift-up effect). These three processes concern primarily disturbances which do not vary in the streamwise direction ($\alpha = 0$). It is well known that for $\alpha \neq 0$, the system is unstable to flow-induced surface instabilities when the wall stiffness is low, or to Tollmien–Schlichting waves when the Reynolds number is large, but

we have chosen here to focus on different mechanisms which might dominate the initial dynamics under specific receptivity conditions. The mechanisms in question are based on the interaction of wall modes, that is the flow/walls structures originating from travelling waves of the flexible plates.

Our main results are summarised by figures 6 and 9. The computed optimal energy growth can be explained from simple system deformations where the Poiseuille flow is displaced in the vertical direction in a sinuous shape, or stretched/contracted in a varicose manner. A quantification of the energy evolution for this simple model shows good agreement with the computed data, thus confirming our description of the mechanisms at play. The period of the standing-wave oscillations can be easily predicted from the dispersion relation of free-wall waves, modified to account for an added mass effect due to the presence of the fluid (cf. equation 3.4).

These mechanisms are most energetic when the walls are very elastic and the forcing disturbance spectrum include long spanwise wavelengths. Under these conditions the compliant channel is sensitive to external perturbations. Note that almost all of the energy growth is carried by the streamwise velocity perturbation, as a result of the up/down advection of the base flow profile. In the case of anisotropic wall properties, where for instance waves which are initially amplified by the exponential mechanism at $\alpha \neq 0$ are eventually damped by an increasing rigidity in the longitudinal direction, the standing wave shown in figure 4 and 5 should dominate the overall system behaviour.

It is now interesting to discuss whether these mechanisms are 'dangerous' in terms of transition to turbulence. The oscillations at infinite wavelength consist of up and down motion of the entire channel plus the walls. The total energy is conserved, but the perturbation with respect to the static reference parabolic profile follows a large amplitude oscillatory evolution. Probably here, as it is also the case for long sinuous waves, the energy growth with respect to the static profile does not imply strong flow distortions (hence no strong secondary instabilities should be expected). For the varicose symmetry on the other hand, the Poiseuille profile is not simply advected up and down, but it is stretched and contracted, in a motion associated with particles flowing from constricted to expanded regions. This distortion is more complex and it is likely that the velocity gradients thus generated be of relevance to transition to turbulence.

The type of analysis presented in this paper, where optimisation is used to put in evidence mechanisms of energy growth, is commonly referred to as *non-modal*. This term might however be misleading here since two spanwise counter-propagating eigenmodes, associated with the traveling waves of the flexible plates, are sufficient to generate a standing wave able to extract energy efficiently from the base flow. In this sense, this *bi-modal* mechanism is different from that discussed for example by Cossu & Chomaz (1997), Schmid & Henningson (2002) and Ehrenstein & Gallaire (2005), whereby eigenmodes can collectively generate transient growth by forming localised wave packets.

Support from the EU in the form of a Marie Curie EST grant (project FLUBIO, MEST-CT-2005-020228) is gratefully acknowledged.

REFERENCES

Benjamin, T. B. 1960 Effects of a flexible boundary on hydrodynamic stability. *J. Fluid Mech.* **9**, 513–532.

Butler, K. M. & Farrell, B. F. 1992 Three-dimensional optimal perturbations in viscous shear flows. *Phys. Fluids* **4** (8), 1637–1650.

Carpenter, P. W., Davies, C. & Lucey, A. D. 2000 Hydrodynamics and compliant walls: does the dolphin have a secret? *Curr. Sci.* **79**, 758–765.

Carpenter, P. W. & Garrad, A. D. 1985 The hydrodynamic stability of flow over Kramer-type compliant surfaces. Part 1. Tollmien–Schlichting instabilities. *J. Fluid Mech.* **155**, 465–510.

Carpenter, P. W. & Garrad, A. D. 1986 The hydrodynamic stability of flow over Kramer-type compliant surfaces. Part 2. Flow-induced surface instabilities. *J. Fluid Mech.* **170**, 199–232.

Carpenter, P. W. & Pedley, T. J., ed. 2003 *Flow Past Highly Compliant Boundaries and in Collapsible Tubes*, *Fluid Mechanics and Its Applications*, vol. 72, IUTAM Symposium. Springer.

Cossu, C. & Chomaz, J.-M. 1997 Global measures of local convective instabilities. *Phys. Rev. Lett.* **78**, 4387–4390.

Davies, C. & Carpenter, P. W. 1997 Instabilities in a plane channel flow between compliant walls. *J. Fluid Mech.* **352**, 205–243.

Domaradzki, J. A. & Metcalfe, R. W. 1987 Stabilization of laminar boundary layers by compliant membranes. *Phys. Fluids* **30** (3), 695–705.

Ehrenstein, U. & Gallaire, F. 2005 On two-dimensional temporal modes in spatially evolving open flows: the flat plate boundary layer. *J. Fluid Mech.* **536**, 209–218.

Fish, F. E. & Lauder, G. V. 2006 Passive and active flow control by swimming fishes and mammals. *Ann. Rev. Fluid Mech.* **38**, 193–224.

Gray, J. 1936 Studies in animal locomotion. VI. the propulsive power of dolphins. *J. Exp. Biol.* **13**, 192–199.

Guaus, A. & Bottaro, A. 2007 Instabilities of the flow in a curved channel with compliant walls. *Proc. R. Soc. A* **463**, 2201–2222.

Gad-el Hak, M. 2000 *Flow control. Passive, active, and reactive flow management*. Cambridge University Press.

Kramer, M. O. 1957 Boundary-layer stabilization by distributed damping. *J. Aerosp. Sci.* **24**, 459–460.

Kramer, M. O. 1960 Boundary-layer stabilization by distributed damping. *J. Am. Soc. Navig. Eng.* **72**, 25–33.

Landahl, M. T. 1962 On the stability of a laminar incompressible boundary layer over a flexible surface. *J. Fluid Mech.* **13**, 609–632.

Nagata, M. & Cole, T. R. 1999 On the stability of plane Poiseuille flow between compliant boundaries. *In Proc. Int. Conf. Computational Methods and Experimental Measurements IX, Naples, Italy (eds G. M. Carlomagno and C. A. Brebbia), Southampton, UK : WIT Press.* pp. 231–240.

Riley, J.J., Gad-el Hak, M. & Metcalfe, R.W. 1988 Compliant coatings. *Ann. Rev. of Fluid Mech.* **20**.

Schmid, P. & Henningson, D. 2002 On the stability of a falling liquid curtain. *J. Fluid Mech.* **463**, 163–171.

Schmid, P. J. & Henningson, D. S. 2001 *Stability and transition in shear flows*. Springer, New York.

Trefethen, L. 2000 *Spectral Methods in Matlab*. SIAM.

Trefethen, L. N., Trefethen, A. E., Reddy, S. C. & Driscoll, T. A. 1993 Hydrodynamic stability without eigenvalues. *Science* **261**, 578–584.

Wiplier, O. & Ehrenstein, U. 2001 On the absolute instability in a boundary-layer flow with compliant coating. *Eur. J. Mech. B - Fluids* **20**, 127–144.